Journal of Cerebral Blood Flow & Metabolism (2011) 31, 648–657

www.jcbfm.com

# Parametric mapping of [$^{18}$F]fluoromisonidazole positron emission tomography using basis functions

Young T Hong[1], John S Beech[2,4], Rob Smith[1], Jean-Claude Baron[3] and Tim D Fryer[1]

[1]*Wolfson Brain Imaging Centre, Department of Clinical Neurosciences, University of Cambridge, Cambridge, UK;* [2]*Division of Anaesthesia, Department of Medicine, University of Cambridge, Cambridge, UK;* [3]*Stroke Research Group, Department of Clinical Neurosciences, University of Cambridge, Cambridge, UK*

**In this study, we show a basis function method (BAFPIC) for voxelwise calculation of kinetic parameters ($K_1$, $k_2$, $k_3$, $K_i$) and blood volume using an irreversible two-tissue compartment model. BAFPIC was applied to rat ischaemic stroke micro-positron emission tomography data acquired with the hypoxia tracer [$^{18}$F]fluoromisonidazole because irreversible two-tissue compartmental modelling provided good fits to data from both hypoxic and normoxic tissues. Simulated data show that BAFPIC produces kinetic parameters with significantly lower variability and bias than nonlinear least squares (NLLS) modelling in hypoxic tissue. The advantage of BAFPIC over NLLS is less pronounced in normoxic tissue. $K_i$ determined from BAFPIC has lower variability than that from the Patlak–Gjedde graphical analysis (PGA) by up to 40% and lower bias, except for normoxic tissue at mid-high noise levels. Consistent with the simulation results, BAFPIC parametric maps of real data suffer less noise-induced variability than do NLLS and PGA. Delineation of hypoxia on BAFPIC $k_3$ maps is aided by low variability in normoxic tissue, which matches that in $K_i$ maps. BAFPIC produces $K_i$ values that correlate well with those from PGA ($r^2 = 0.93$ to 0.97; slope 0.99 to 1.05, absolute intercept $< 0.00002$ mL/g per min). BAFPIC is a computationally efficient method of determining parametric maps with low bias and variance.**
*Journal of Cerebral Blood Flow & Metabolism* (2011) **31,** 648–657; doi:10.1038/jcbfm.2010.141; published online 25 August 2010

**Keywords:** basis function; [$^{18}$F]fluoromisonidazole; FMISO; kinetic modelling; parametric mapping; positron emission tomography

## Introduction

[$^{18}$F]fluoromisonidazole (FMISO) positron emission tomography (PET) has been used for *in vivo* imaging of hypoxia in tumours (Koh *et al*, 1992; Rasey *et al*, 1996; Bruehlmeier *et al*, 2004; Thorwarth *et al*, 2005, 2006; Rajendran *et al*, 2006; Eschmann *et al*, 2007; Wang *et al*, 2010), ischaemic myocardium (Martin *et al*, 1992), and stroke (Markus *et al*, 2004; Takasawa *et al*, 2007, 2008; Spratt *et al*, 2009). FMISO is a nitromidazole compound that diffuses freely through cell membranes and binds in hypoxic cells (Chapman *et al*, 1989; Casciari *et al*, 1995).

Most FMISO PET studies have used late imaging, with 2 to 4 hours postinjection being considered optimal because of the passive transport and slow reaction mechanism (Koh *et al*, 1992). These late images are then quantified through conversion to standardised uptake value (Thorwarth *et al*, 2006), tissue-to-blood ratio (Koh *et al*, 1992) or tissue-to-muscle ratio (Eschmann *et al*, 2007). To determine more specific information, both reversible (Bruehlmeier *et al*, 2004; Kelly and Brady, 2006) and irreversible (Casciari *et al*, 1995; Thorwarth *et al*, 2005; Wang *et al*, 2009, 2010) compartment models have been proposed to model FMISO kinetics.

Bruehlmeier *et al* (2004) applied both Logan graphical analysis (Logan *et al*, 1990) and a two-tissue reversible compartment model to tumour FMISO data, and Kelly and Brady (2006) also used this model on

Correspondence: Dr TD Fryer, Wolfson Brain Imaging Centre, Box 65, Addenbrooke's Hospital, Hills Road, Cambridge CB2 0QQ, UK.
E-mail: tdf21@wbic.cam.ac.uk
[4]Current address: Gray Institute for Radiation Oncology and Biology, University of Oxford, Oxford, UK.
*Financial support*: YTH and RS are funded by the Wolfson Brain Imaging Centre Major Research Facility, JSB was funded by the University of Cambridge Clinical School, and JCB and TDF are funded by the Higher Education Funding Council for England (HEFCE). This study was supported by a Medical Research Council (MRC) grant (G0001219) awarded to JCB. Equipment used for the stroke procedure was funded by a grant from Pfizer UK to JSB and the microPET P4 scanner was partially funded by Merck Sharp and Dohme.
Received 19 March 2010; revised 17 June 2010; accepted 27 July 2010; published online 25 August 2010

simulated data, with an extra parameter to model spatial diffusion of free FMISO and its reduced compounds. Casciari *et al* (1995) developed a comprehensive irreversible kinetic model that consists of four tissue compartments and seven model parameters, three of which were fixed to make the model more robust. Thorwarth *et al* (2005) presented an irreversible two-tissue compartment model with a reference tissue input which obviates blood sampling and Wang *et al* (2009) used a plasma input two-tissue irreversible compartment model on simulated data. Subsequently, Wang *et al* (2010) used this model combined with an image-based plasma input function for the analysis of clinical FMISO data.

For our FMISO data obtained in an ischaemic stroke model in the rat, Patlak–Gjedde graphical analysis (PGA, Gjedde, 1982; Patlak *et al*, 1983) indicated an irreversible kinetic model and regional kinetic modelling with a two-tissue irreversible model provided good fits to the data (Takasawa *et al*, 2007). Kinetic modelling at the voxel level has a number of advantages over its regional counterpart: it maximises the information obtained on the spatial distribution of tracer kinetics; the use of a kinetic model designed for the homogeneous tissue is more valid for voxelwise modelling; the production of parametric maps allows any subsequent region-of-interest (ROI) analysis to be tailored to kinetically homogeneous regions if required; applications such as PET-guided radiotherapy require parametric maps rather than regional information. However, the key problem with voxelwise modelling is the high noise level. For irreversible tracers, influx rate ($K_i$) can be determined with PGA, which is robust against noise. A disadvantage of $K_i$ is that it is affected by tracer delivery and washout, as well as by tracer accumulation in the tissue. Compartment modelling allows these factors to be decoupled, which is especially of interest if the rate of tracer accumulation is a key parameter, as for FMISO because it can be related to tissue oxygen concentration (Casciari *et al*, 1995).

Determination of rate constants using nonlinear least squares solution (NLLS) of compartmental models is highly sensitive to noise and hence not suited to voxelwise modelling. In this study, we provide a basis function solution of the irreversible two-tissue compartment model. Parametric mapping with basis functions based on compartment models has been used previously for a reversible one-tissue compartment model (Koeppe *et al*, 1985; Lodge *et al*, 2000; Boellaard *et al*, 2005; Watabe *et al*, 2005), for reference tissue modelling (Gunn *et al*, 1997; Wu and Carson, 2002) and for the production of [18F]fluorodeoxyglucose (FDG) $K_i$ maps with two-tissue compartment models (Hong and Fryer, 2010). This study illustrates the latter approach for FMISO $K_1$, $k_2$, $k_3$, $V_b$ and $K_i$ mapping using an irreversible two-tissue compartment model with a plasma input function. The bias-noise properties of the basis function method (BAFPIC) are compared with those of NLLS and PGA using simulated FMISO data. These methods are also assessed with real FMISO microPET data.

# Materials and methods

## Kinetic Modelling

*Basis Function Solution of a Two-Tissue Irreversible Compartment Model (BAFPIC)*: For a two-tissue compartment model of an irreversible tracer, the total radioactivity concentration is given by

$$C_T = (1 - V_b)(C_r + C_i) + V_b C_b \tag{1}$$

where $V_b$ is the fractional blood volume in the tissue, $C_r$ the concentration in the reversible tissue compartment, $C_i$ the concentration in the irreversibly trapped compartment, and $C_b$ the concentration in whole blood. It should be noted that for clarity, the time dependence of the concentrations has been omitted.

The temporal behaviour of the above model is given by

$$\begin{aligned} \frac{dC_r}{dt} &= K_1 C_a - (k_2 + k_3) C_r \\ \frac{dC_i}{dt} &= k_3 C_r \end{aligned} \tag{2}$$

where $K_1$ (mL/g per min) is the transport rate constant of tracer from the plasma to the tissue, $k_2$ (1/min) the efflux rate constant from the tissue to the plasma, $k_3$ (1/min) the rate constant into the irreversibly trapped state, and $C_a$ the tracer concentration in arterial plasma.

Solution of the differential equations in equation (2) allows equation (1) to be rewritten as

$$C_T = \frac{(1 - V_b)K_1}{\alpha} \left[k_3 + k_2 e^{-\alpha t}\right] \otimes C_a + V_b C_b \tag{3}$$

where $\alpha = k_2 + k_3$. Equation (3) can be parameterised as

$$C_T = (\theta_1 + \theta_2 e^{-\alpha t}) \otimes C_a + V_b C_b \tag{4}$$

Basis functions (e.g., $N = 100$) can be precalculated for the nonlinear term in equation (4) using a physiologically feasible range of $\alpha$

$$B_j = e^{-\alpha_j t} \otimes C_a \qquad j = 1, \ldots, N \tag{5}$$

The range of $\alpha$ is tracer specific and based on values obtained from regional kinetic modelling of FMISO in an ischaemic stroke rat model, 100 basis functions with logarithmically spaced $\alpha = [0.01,\ 0.1]$ 1/min were used. With the inclusion of a diagonal matrix of weights $W$, calculated using the scheme of Gunn *et al* (1997), equation (4) can be written for each basis function as

$$WC_T = A_j \begin{bmatrix} \theta_1 \\ \theta_2 \\ V_b \end{bmatrix}_j \tag{6}$$

where

$$A_j = W\left[\int C_a \quad B_j \quad C_b\right] \tag{7}$$

The use of basis functions allows the linear solution of equation (6)

$$\begin{bmatrix} \theta_1 \\ \theta_2 \\ V_b \end{bmatrix}_j = A_j^{-1} W C_T \tag{8}$$

To obtain the inverse of $A_j$, QR decomposition (Householder, 1970) was used

$$A_j^{-1} = R_j^{-1} Q_j^T \tag{9}$$

where $R_j$ is a right triangular matrix and $Q_j$ an orthogonal matrix. From the set of $N$ solutions, the one with the lowest weighted residual sum of squares was chosen.

Individual kinetic parameters can then be obtained

$$K_1 = \frac{\theta_1 + \theta_2}{1 - V_b} \quad (10)$$

$$k_2 = \frac{\theta_2 \alpha}{\theta_1 + \theta_2} \quad (11)$$

$$k_3 = \frac{\theta_1 \alpha}{\theta_1 + \theta_2} \quad (12)$$

$$K_i = \frac{\theta_1}{1 - V_b} \quad (13)$$

*Nonlinear Least Squares Compartmental Modelling*: For both simulated and real FMISO data, individual kinetic rate constants and $V_b$ were determined from equation (3) using nonlinear weighted least squares fitting optimised with the Levenberg–Marquardt method (Marquardt, 1963), using the same weighting scheme as used for the basis function fitting. $K_i$ was then determined from Gjedde (1982)

$$K_i = \frac{K_1 k_3}{k_2 + k_3} \quad (14)$$

*Patlak–Gjedde Graphical Analysis*: $K_i$ was determined using linear least squares (LLS) fitting to transformed data (Gjedde, 1982; Patlak *et al*, 1983) for both simulated and real FMISO data. In all cases, tissue data from 75 minutes onwards were used.

### Simulated [18F]Fluoromisonidazole Data

Hypoxic and normoxic time–activity curves (TACs) were generated from kinetic parameters determined by NLLS fitting to ROI data from an ischaemic stroke rat microPET study using a permanent distal middle cerebral artery occlusion (MCAo; Takasawa *et al*, 2007). The ROI (20.3 $mm^3$) was defined with an intensity threshold in the hypoxic region of the summed FMISO image. It was then moved to a similar position in the contralateral hemisphere to determine the normoxic TAC. The kinetic parameters from the NLLS fits were: hypoxic: $K_1 = 0.0247$ mL/g per min, $k_2 = 0.0191$ 1/min, $k_3 = 0.0218$ 1/min, $V_b = 0.0407$ and normoxic: $K_1 = 0.0423$ mL/g per min, $k_2 = 0.0487$ 1/min, $k_3 = 0.0020$ 1/min, $V_b = 0.0549$.

Monte Carlo simulation with 1,000 realisations per noise level was performed to test the bias and variability of BAFPIC against NLLS and PGA. Noise with a Gaussian distribution ($\mu = 0$, $\sigma^2 = \beta(\overline{C_T}(t_i)/\Delta t_i)$) was added to the TACs, where $\beta$ had 20 values spaced linearly in the range [0.001, 0.65], $\overline{C_T}$ is the average of the hypoxic and normoxic TACs at mid-frame time $t_i$, and $\Delta t_i$ the duration of time frame $i$. The use of $\overline{C_T}$ in the noise model is appropriate as the filtered backprojection algorithm used to reconstruct the real data results in a noise level that is not dictated by the local voxel value (Barrett *et al*, 1994). The simulation was performed for the same protocol used for real microPET experiments: 80 time frames over 3 hours ($24 \times 5$ seconds, $6 \times 30$ seconds, $15 \times 60$ seconds, $5 \times 120$ seconds, and $30 \times 300$ seconds).

For NLLS, the initial parameter estimates for fits to both hypoxic and normoxic TACs were: $K_1 = 0.035$ mL/g per min, $k_2 = 0.035$ 1/min, $k_3 = 0.01$ 1/min and $V_b = 0.04$. These values represent reasonable estimates in the absence of information on the degree of hypoxia, as would be the case with real data. The weights for BAFPIC and NLLS used the average TAC, $\overline{C_T}$, within the scheme of Gunn *et al* (1997) in lieu of true coincidences.

### microPET [18F]Fluoromisonidazole Rat Data

Data from two rats were used: the permanent MCAo rat and a control rat from the data set described in the study by Takasawa *et al* (2007). Parametric maps were generated for both rats and the permanent MCAo rat was also used to produce regional data from which the aforementioned simulated data were derived.

Animal experiments were performed in accordance with the UK Home Office guidelines and with the approval of the University of Cambridge Animal Ethical Review Panel. Male spontaneous hypertensive rats (Charles River Laboratory, Margate, UK) were used. The experimental procedures are detailed in the study by Takasawa *et al* (2007).

As the data acquisition was described in detail in Takasawa *et al* (2007), brief details are given here. List-mode PET data were acquired using a microPET P4 scanner (Concorde Microsystems, Knoxville, TN, USA) (Tai *et al*, 2001) after ~80 MBq of FMISO in 1 mL was injected intravenously as a bolus over 30 seconds using an automated syringe driver. For the MCAo rat, the tracer was administered 39 minutes after the start of MCAo. In Takasawa *et al* (2007), the list-mode data were histogrammed into 60 time frames, but in this study, data from the first 5 minutes were histogrammed into shorter time frames to produce 80 time frames in total, with durations as described above for the simulated data. Emission data acquisition was followed by windowed coincidence mode transmission scans for attenuation correction (acquisition time: 20 minutes) with a rotating $^{68}Ge/^{68}Ga$ point source.

The images were reconstructed into $0.5 \times 0.5 \times 0.5$ $mm^3$ voxels using the PROMIS three-dimensional filtered back-projection algorithm (Kinahan and Rogers, 1989), with corrections for randoms, dead time, background, normalisation, attenuation, sensitivity and decay applied.

Arterial blood samples were collected from two control rats to obtain average plasma and whole-blood input functions. For other rats, to limit blood loss, 4 arterial blood samples were taken at 30, 60, 120, and 180 minutes after FMISO injection and these samples were used to scale the input function from control rats.

For NLLS, the initial parameter estimates were the same as for the simulated data. The weights used for BAFPIC and NLLS were based on true coincidences, obtained

by subtracting delayed coincidences from prompts, as described by Gunn *et al* (1997).

Voxelwise parametric mapping was constrained to brain tissue through the use of a binary mask derived from a coregistered magnetic resonance (MR) scan. The correlation between parameters estimated at the voxel level was quantified using the Pearson correlation coefficient.

## Results

### Evidence of Irreversible Trapping of [18F]Fluoromisonidazole

Figure 1A shows Patlak plots for hypoxic and normoxic regional TACs from the MCAo rat used to produce the simulated data. Linear regions are found for data >75 minutes after injection, indicating irreversible trapping. The hypoxic and normoxic $K_i$ values are 0.0123 and 0.0011 mL/g per min, respectively.

### Evidence Supporting the Validity of the Irreversible Two-Tissue Compartment Model

Figure 1B shows the TACs used in Figure 1A and the corresponding NLLS fits. These data support the use of the irreversible two-tissue compartment model (equation (3)). The kinetic parameters and blood volumes obtained from the NLLS fits were those used to produce the simulated data.

### Simulated [18F]Fluoromisonidazole Data

Figure 2 gives bias-variability plots for $K_1$, $k_2$, $k_3$, and $V_b$ estimated by BAFPIC and NLLS for the simulated hypoxic and normoxic TACs. Values from Figure 2 at the noise level that best corresponds to the real data (at noise level 11) are given in Table 1. This noise level was determined through visual inspection of simulated and real TACs, and by comparing the residual sum of squares from model fitting to the TACs. The variability of NLLS is significantly inferior to BAFPIC for hypoxic tissue, much less so for normoxic tissue. It should be noted that for a number of the plots in Figure 2, the variability of NLLS, especially for hypoxic tissue, is so high that a number of the 20 data points lie outside the plot. The instability of NLLS results in high biases for $K_1$, $k_2$ and $k_3$ in hypoxic tissue. For BAFPIC, comparable variability is found for hypoxic and normoxic tissues, with the most notable exception being much lower variability for $k_3$ in normoxic tissue than in hypoxic tissue.

Some noise-induced bias is found for BAFPIC, most notably for $k_2$ in hypoxic tissue (Figure 2B) and $k_3$ (Figure 2C). The cause of this bias is positive bias of $\alpha$, leading to positive bias of $\theta_2$; the $\alpha$-spectra in Supplementary Figure 1 for noise level 11 have mean values that are 2 and 12% high for normoxic and

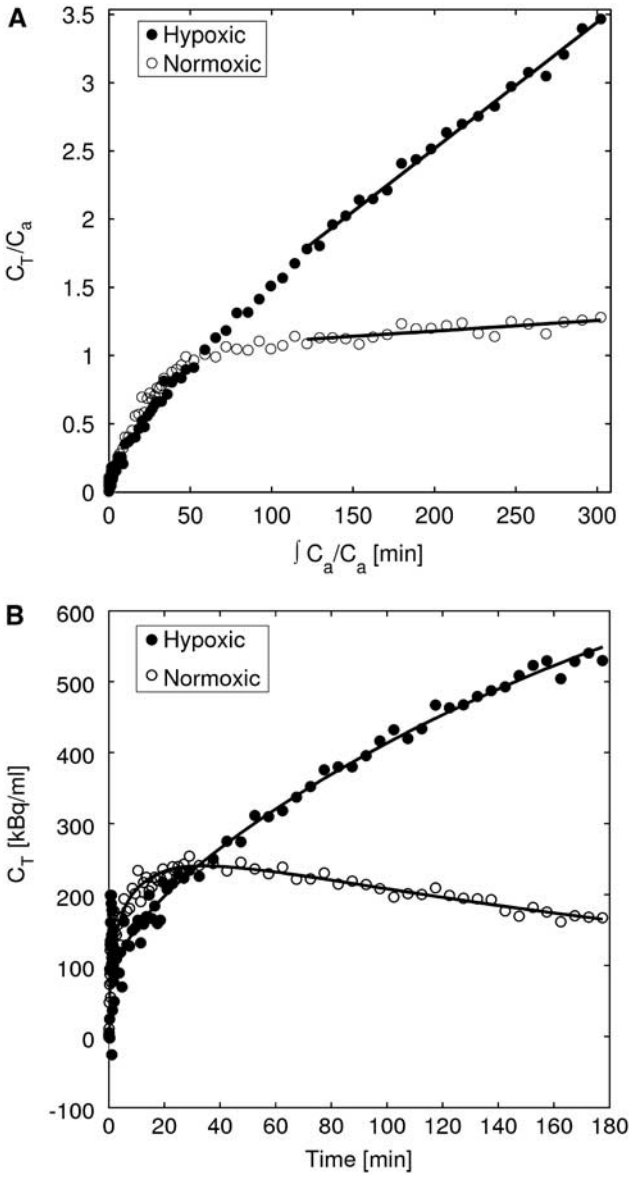


**Figure 1** Patlak–Gjedde plots and time-activity curves for hypoxic and normoxic tissue. (**A**) Patlak–Gjedde plot of hypoxic and normoxic regional data with the linear region indicating an irreversible compartment and (**B**) irreversible two-tissue compartmental model fit to the hypoxic and normoxic regional data. $C_T$, decay-corrected total radioactivity concentration in the tissue; $C_a$, decay-corrected radioactivity concentration in arterial plasma.

hypoxic tissues, respectively. For hypoxic tissue, the main bias is found for $k_2$ because the numerator of equation (11) is the product of two positively biased parameters ($\theta_2\alpha$), whereas for normoxic tissue, a negative bias is found for $k_3$ (equation (12)) because the small positive bias in $\theta_2$ leads to a larger compensatory negative percentage bias in $\theta_1$ because $\theta_2 \gg \theta_1$.

$K_i$ values determined from the simulated data by BAFPIC, NLLS, and PGA are also shown in Figure 2 and in Table 1. For both tissue types, BAFPIC has the

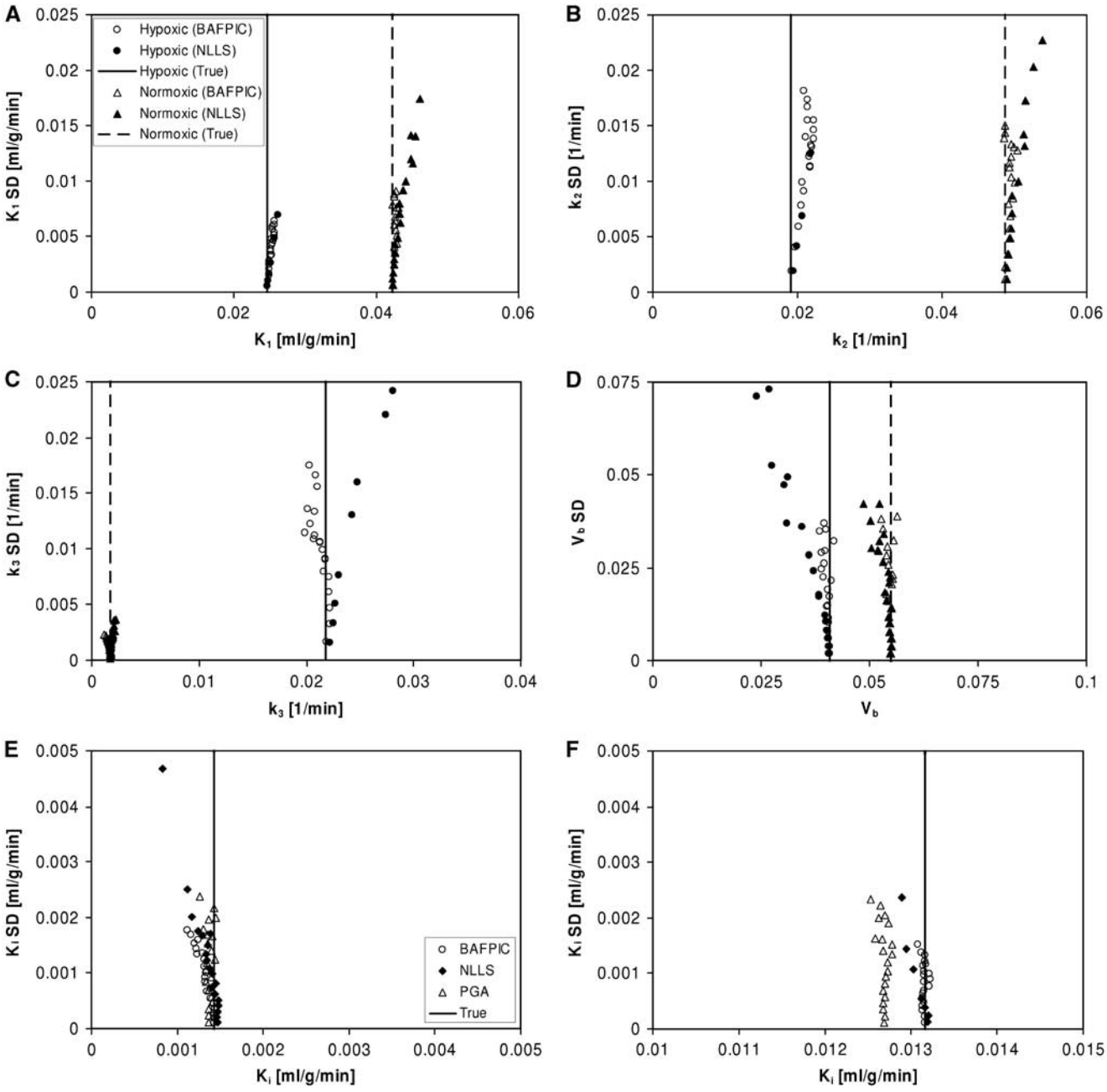


**Figure 2** Bias-variability plots of kinetic parameters estimated from simulated hypoxic and normoxic data. (**A** to **D**) Parameters estimated by BAFPIC and NLLS: (panel **A**) $K_1$, (panel **B**) $k_2$, (panel **C**) $k_3$, and (panel **D**) $V_b$. (**E** to **F**) $K_i$ estimated by BAFPIC, NLLS, and PGA for (panel **E**) normoxic and (panel **F**) hypoxic data. The vertical lines indicate the true parameter values. The legend shown in plot **A** is applicable to plots **A** to **D**, whereas that shown in plot **E** is also applicable to plot **F**. BAFPIC, basis function method; NLLS, nonlinear least squares; PGA, Patlak–Gjedde graphical analysis; SD, standard deviation.

lowest variability, up to 40% lower than for PGA. Variability for NLLS is comparable with that for BAFPIC and PGA in normoxic tissue but significantly higher in hypoxic tissue, consistent with the variability found for $K_1$, $k_2$ and $k_3$ with NLLS. The BAFPIC has the lowest bias for hypoxic and normoxic tissues at low noise, but the highest bias for normoxic tissue in the middle noise levels—as for $k_3$, this bias in $K_i$ (equation (13)) is caused by negative bias of $\theta_1$. Overall, PGA gives the best bias performance for $K_i$ in normoxic tissue.

### microPET [18F]Fluoromisonidazole Rat Data

Figures 3 and 4 show parametric maps for a MCAo rat and a control rat, respectively. $K_1$, $k_2$, $k_3$, and $V_b$ maps are given for NLLS and BAFPIC, and $K_i$ is

**Table 1** Bias and s.d. values for kinetic parameters estimated at noise level 11 of the simulated data

| | | *Normoxic tissue* | | *Hypoxic tissue* | |
|---|---|---|---|---|---|
| *Parameter* | *Method* | *Bias (%)* | *s.d.* | *Bias (%)* | *s.d.* |
| $K_1$ | NLLS | 2.2 | 0.0080 | 57.9 | 0.0764 |
| | BAFPIC | 0.4 | 0.0061 | 2.8 | 0.0042 |
| $k_2$ | NLLS | 5.7 | 0.0173 | 559.9 | 0.5384 |
| | BAFPIC | 1.1 | 0.0112 | 15.2 | 0.0131 |
| $k_3$ | NLLS | 7.6 | 0.0017 | 77.1 | 0.1609 |
| | BAFPIC | −5.0 | 0.0015 | −2.4 | 0.0106 |
| $V_b$ | NLLS | −0.5 | 0.0226 | −11.5 | 0.0283 |
| | BAFPIC | 0.9 | 0.0219 | 1.0 | 0.0217 |
| $K_i$ | NLLS | −5.8 | 0.0012 | 22.4 | 0.1013 |
| | BAFPIC | −6.7 | 0.0010 | 0.4 | 0.0009 |
| | PGA | −2.6 | 0.0012 | −2.9 | 0.0013 |

BAFPIC, basis function method; NLLS, nonlinear least squares; PGA, Patlak–Gjedde graphical analysis.
s.d., standard deviation units: $K_1$ and $K_i$ (mL/g per min), $k_2$ and $k_3$ (1/min), $V_b$ unitless.

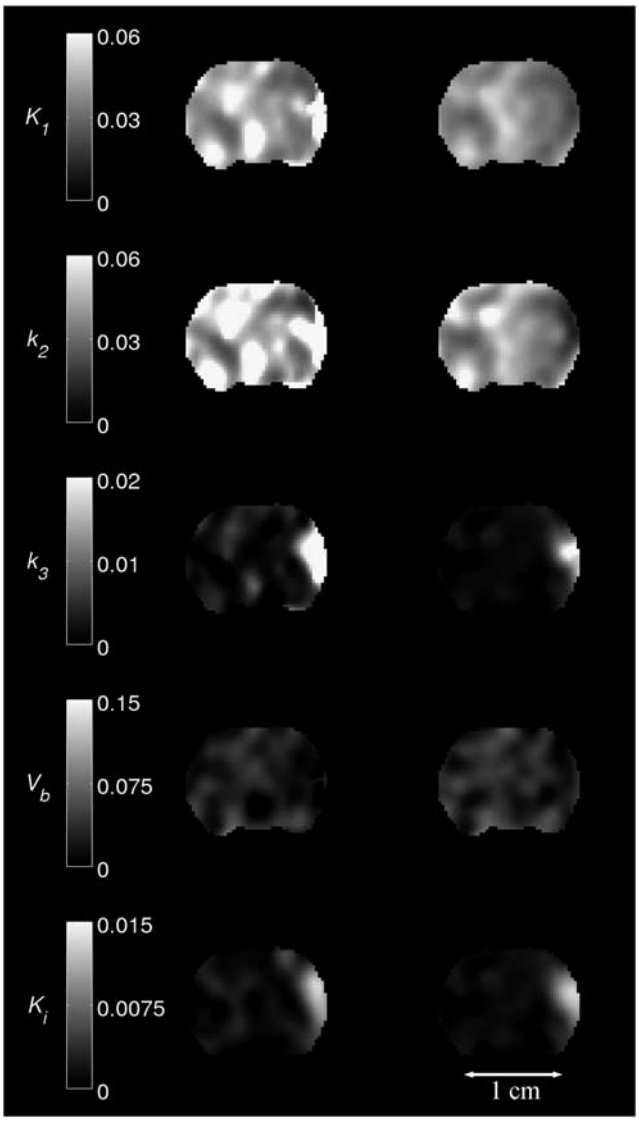


**Figure 3** Parametric maps of $K_1$, $k_2$, $k_3$, $V_b$ and $K_i$ for a MCAo rat. Images in the left-hand column were produced by NLLS ($K_1$, $k_2$, $k_3$ and $V_b$) and PGA ($K_i$); the right-hand column shows the corresponding images for BAFPIC. Scale bar units: $K_1$ and $K_i$ (mL/g per min); $k_2$ and $k_3$ (1/min); $V_b$ unitless. BAFPIC, basis function method; MCAo, middle cerebral artery occlusion; NLLS, nonlinear least squares; PGA, Patlak–Gjedde graphical analysis.

shown for PGA and BAFPIC. The PET images for each rat were coregistered to a template MR image and the same coronal slice is shown in the two figures.

In Figure 3, MCAo occurred on the right-hand side of images and the expected patterns of reduced $K_1$ and $k_2$ are seen in the affected cortex with BAFPIC. For NLLS, reductions in $K_1$ and $k_2$ are seen superiorly, but in the focus of the occlusion, large $K_1$ and $k_2$ increases are seen. This is consistent with the findings of the simulated data where large positive biases for $K_1$ and $k_2$ were seen with NLLS in hypoxic tissue (Table 1). Both NLLS and BAFPIC show that $k_3$ is increased in the MCAo cortex, with the $k_3$ increase for NLLS being much larger than that for BAFPIC, again consistent with the positive bias found with NLLS for $k_3$ in simulated hypoxic tissue (Table 1). The $k_3$ increase for BAFPIC is consistent with the $K_i$ increases seen for both PGA and BAFPIC, although the $k_3$ increase is slightly more focal. This is not unexpected as a reduction in $k_2$ which is greater than that in $K_1$, as observed, will increase $K_i$ unless $k_3$ is also reduced (see equation (14)). Therefore, part of the increased $K_i$ domain seen with both PGA and BAFPIC can be attributed to increased $K_1/k_2$ rather than to an increase in $k_3$. In the unaffected hemisphere, BAFPIC has less variability than both NLLS for $K_1$, $k_2$, $k_3$, and $V_b$ and PGA for $K_i$, again consistent with the findings of the simulated data.

The control rat in Figure 4 does not exhibit the asymmetric changes in kinetic parameters seen with the MCAo rat. As for the unaffected hemisphere of the MCAo rat, the spatial variability of the kinetic parameters for the control rat is lower for BAFPIC than for NLLS and PGA.

Table 2 shows the correlations between parameters estimated at the voxel level by BAFPIC for MCAo and control rats within a region (4,357 voxels) delineated in the hypoxic area of the MCAo rat with $K_i > 30\%$ of the maximum. For both rats, the correlations are high between $K_1$ and $k_2$ ($r = 0.90$ to 0.92) and between $k_3$ and $K_i$ ($r = 0.71$ to 0.85), with the highest of these correlations being in the MCAo rat. In addition, for the MCAo rat, high negative correlations are found between $K_1/k_2$ and both $K_1$ ($r = -0.69$) and $k_2$ ($r = -0.82$), and a mild correlation ($r = 0.41$) is found between $K_1/k_2$ and $K_i$. The increase in $K_1/k_2$ inferred by these data, together with the increased correlation between $K_1/k_2$ and $K_i$ substantiate the idea that part of the increase in $K_i$ in the affected cortex of the MCAo rat is attributed to increased $K_1/k_2$.

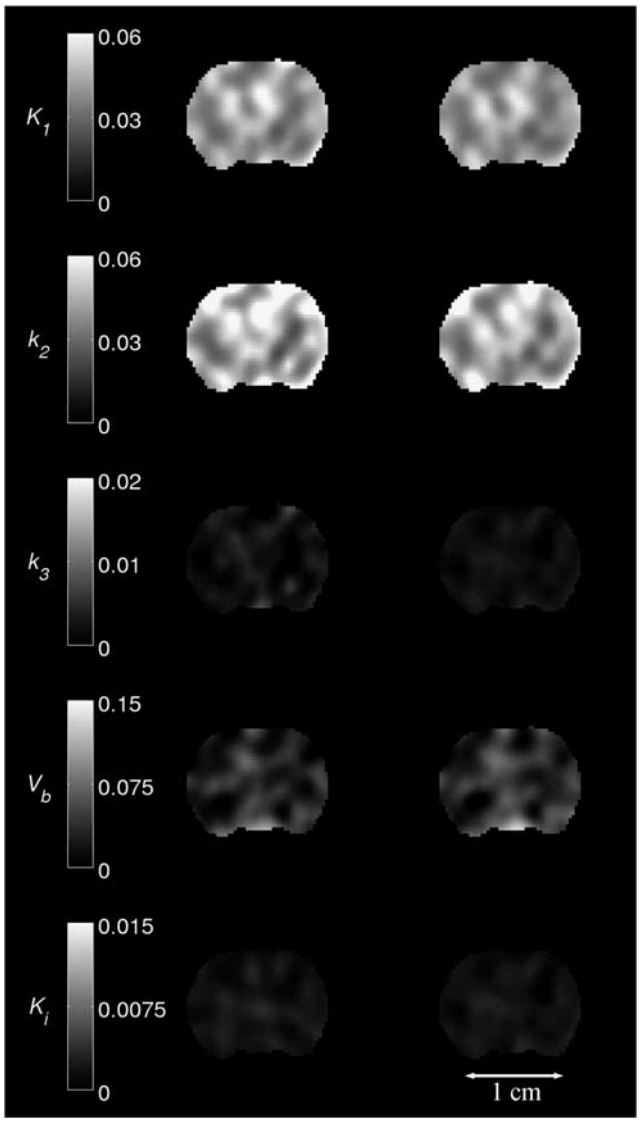


**Figure 4** Parametric maps of $K_1$, $k_2$, $k_3$, $V_b$ and $K_i$ for a control rat. Images in the left-hand column were produced by NLLS ($K_1$, $k_2$, $k_3$ and $V_b$) and PGA ($K_i$), the right-hand column shows the corresponding images for BAFPIC. Scale bar units: $K_1$ and $K_i$ (mL/g per min); $k_2$ and $k_3$ (1/min); $V_b$ unitless. BAFPIC, basis function method; NLLS, nonlinear least squares; PGA, Patlak–Gjedde graphical analysis.

Figure 5 shows the correlation between voxel $K_i$ values obtained with BAFPIC and PGA for both the MCAo rat and the control rat. The correlation plots used 9,091 voxels within the MR brain mask on 12 contiguous coronal slices with enhanced $K_i$ for the MCAo rat. Slopes near to unity are found for both rats; because of the inclusion of blood volume correction with BAFPIC (equation (13)), $K_i$ values ~5% higher than PGA are to be expected. As the bulk of the voxels for the MCAo rat are normoxic, the correlation pattern seen with the control rat is apparent at low $K_i$ values for the MCAo rat.

**Table 2** Correlation matrix for parameters estimated with BAFPIC for MCAo and control rats

| *Rat* | | $K_1$ | $k_2$ | $k_3$ | $V_b$ | $K_i$ | $K_1/k_2$ |
|---|---|---|---|---|---|---|---|
| MCAo | $K_1$ | 1 | 0.92 | 0.00 | −0.15 | −0.26 | −0.69 |
| | $k_2$ | | 1 | 0.16 | −0.14 | −0.23 | −0.82 |
| | $k_3$ | | | 1 | −0.10 | 0.85 | −0.03 |
| | $V_b$ | | | | 1 | −0.10 | 0.07 |
| | $K_i$ | | | | | 1 | 0.41 |
| | $K_1/k_2$ | | | | | | 1 |
| Control | $K_1$ | 1 | 0.90 | 0.17 | 0.17 | −0.28 | −0.34 |
| | $k_2$ | | 1 | 0.33 | 0.20 | −0.32 | −0.35 |
| | $k_3$ | | | 1 | 0.23 | 0.71 | −0.12 |
| | $V_b$ | | | | 1 | 0.29 | −0.29 |
| | $K_i$ | | | | | 1 | 0.10 |
| | $K_1/k_2$ | | | | | | 1 |

BAFPIC, basis function method; MCAo, middle cerebral artery occlusion.
$P < 0.001$ for all correlations shown.

## Discussion

Both reversible and irreversible models have previously been used for FMISO. The key difference between the model given by Casciari *et al* (1995) and that used for BAFPIC here is the addition by Casciari *et al* of two compartments to model diffusible FMISO products in the cell and extracellular space. This diffusion pathway provides another means of tissue signal loss in addition to the reversible loss of FMISO itself. Although the model structure is different from that of Casciari *et al*, Bruehlmeier *et al* (2004) and Kelly and Brady (2006) both used a reversible two-tissue compartment model that allows for the loss of FMISO products. However, Kelly and Brady (2006) only applied their reversible model to simulated data, and in three of the seven patients studied by Bruehlmeier *et al* (2004), an irreversible model ($k_4 = 0$) was sufficient to model the data. Irreversible models have also been applied by Thorwarth *et al* (2005) and by Wang *et al* (2009, 2010). Patlak–Gjedde graphical analysis of our data indicated the existence of an irreversible compartment (Figure 1A) and an irreversible two-tissue compartment model was found to fit both hypoxic and normoxic tissue TACs (Figure 1B).

Kelly and Brady (2006) also modelled the spatial effects of diffusion of FMISO products in their reversible two-tissue compartment model. However, the diffusivity coefficient of misonidazole used by Kelly and Brady ($5.5 \times 10^{-11}$ m$^2$/sec) would result in a diffusion distance of 0.43 mm during a 3-hour PET scan. This is small compared with the resolution of the microPET P4 used in this study: 2.3 mm full-width half-maximum (FWHM) with a Hanning window cutoff at the Nyquist frequency (2.0 1/mm). Combining these two numbers in quadrature yields 2.34 mm FWHM, a negligible increase in effective spatial resolution. For human imaging, the impact of diffusion will be even less because of the poorer spatial resolution of clinical PET scanners (~5 mm

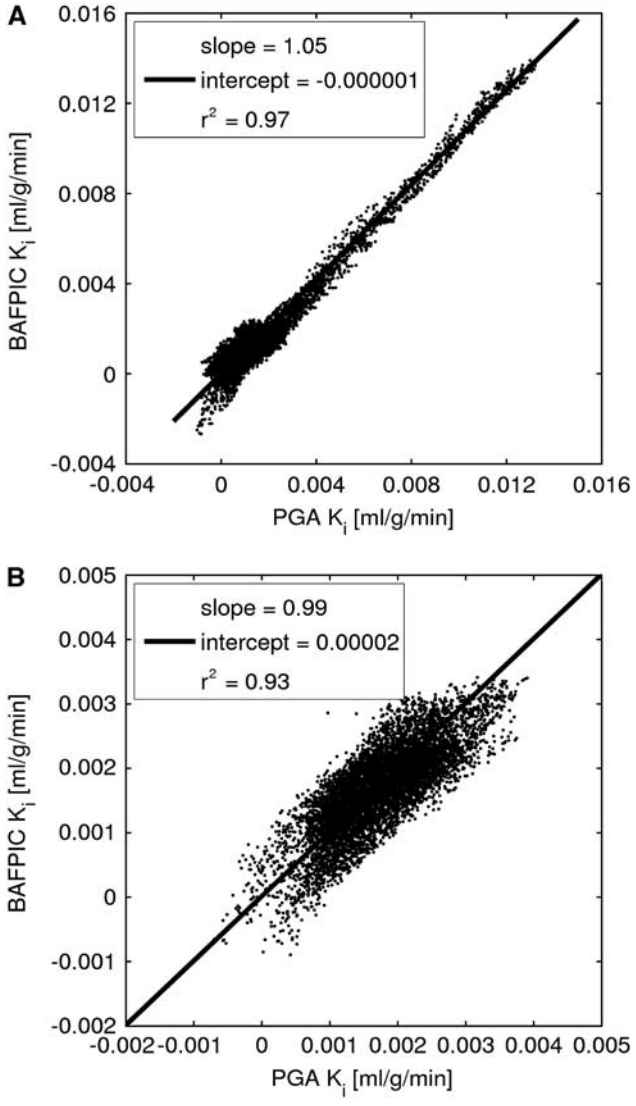


**Figure 5** Correlation of $K_i$ from BAFPIC and PGA. (**A**) MCAo rat shown in Figure 3 and (**B**) control rat shown in Figure 4. The same voxels ($n = 9{,}091$) were used for both panels **A** and **B**. BAFPIC, basis function method; MCAo, middle cerebral artery occlusion; PGA, Patlak–Gjedde graphical analysis.

FWHM). On the basis of this, together with the fits to our data and the use of irreversible models by others, we ignored the kinetic and spatial effects of diffusion in our model.

Voxelwise modelling of rate constants for two-tissue compartment models has been performed previously by LLS (Blomqvist, 1984), constrained LLS (Huang *et al*, 2007), generalised LLS with clustering based on principal components (Kimura *et al*, 2002), and nonlinear ridge regression with spatial constraint (Zhou *et al*, 2002). Blomqvist (1984) and Kimura *et al* (2002) ignored blood volume, Huang *et al* (2007) applied blood volume correction using a cluster value, and Zhou *et al* (2002) produced maps of blood volume. Feng *et al* (1995) showed that the estimates from the LLS algorithm are biased and consequently extended the method to generalised LLS, which was shown for FDG to have bias and variance properties similar to NLLS. To reduce the variability found with generalised LLS, Kimura *et al* (2002) combined it with clustering based on the principal components of TACs and applied the technique to FDG. For an irreversible two-tissue compartment model (with blood volume neglected), the clustering technique reduced variability by 23 and 33% for $K_i$ and $k_3$, respectively. As a direct comparison, in Hong and Fryer (2010), BAFPIC reduced FDG $K_i$ variability by $\sim$60% compared with NLLS in the simulated grey matter at clinically realistic noise levels, indicating the impressive noise reduction properties of BAFPIC, which matched those of nonlinear ridge regression with spatial constraint applied to FDG (Zhou *et al*, 2002). Zhou *et al* (2002) obtained reductions in FDG $k_3$ variability of $\sim$70%, whereas Huang *et al* (2007) reported corresponding reductions of 34%. As the tracer and physiology are different, the variability reductions quoted above cannot be directly related to those reported in this study on FMISO, in which BAFPIC reduced $K_i$ variability compared with NLLS by 18 and 99% in normoxic and hypoxic tissues, respectively, with corresponding reductions in $k_3$ variability of 15 and 93% (Table 1). However, the values for FDG with similar kinetic models put the reported FMISO values into some context because there are no corresponding published numbers for voxelwise FMISO kinetic modelling, the closest being illustrative uptake at infinite time ($S_\infty$) maps of head and neck cancer patients in Thorwarth *et al* (2005), and $K_i$ and $K_1$ maps in Wang *et al* (2010) also in head and neck cancer.

The improvement in variability and bias offered by BAFPIC over NLLS is considerably higher for hypoxic than for normoxic tissue (Figure 2 and Table 1). This is likely to be because of the fact that normoxic tissue is dominated by two kinetic parameters ($K_1$ and $k_2$) as $k_3 \ll k_2$, whereas in hypoxic tissue, $k_3$ is comparable with $k_2$. The effective reduction in the numbers of free parameters from four to three for normoxic tissue results in a dramatic increase in stability for NLLS. In hypoxic tissue found in the stroke model, which has reductions in $K_1$ and $k_2$, NLLS is totally unreliable at realistic noise levels, with the exception of blood volume estimation. In contrast, BAFPIC shows the expected patterns of reduced $K_1$ and $k_2$, together with increased $k_3$ in the affected, i.e., ischaemic and hypoxic, cortex (Figure 3). However, even for BAFPIC, the parametric images of real data shown in Figures 3 and 4 are subjected to blotchy noise artefacts, especially for $k_2$, $V_b$, and $K_1$. It is important to note that even the $K_i$ maps produced by PGA have the artefacts, which are attributed to the spatial correlation of noise by the filtered backprojection algorithm propagating into the parametric maps. The artefacts are so pronounced because the height and width of the brain in these images is only 10 and 13 mm, respectively, which is only $\sim$5 times the spatial resolution. In a human brain image, this factor is $\sim$30; hence, spatially correlated noise from the reconstruction process is less apparent.

Correlation analysis shows that only two pairs of the parametric maps produced by BAFPIC for real FMISO microPET data have strongly correlated voxel values: $K_1$ and $k_2$; $k_3$ and $K_i$ (Table 2). The high correlation between $K_1$ and $k_2$ is to be expected because it is consistent with matched tissue influx and efflux, although in the affected cortex of the MCAo rat, significant negative correlations are found between $K_1/k_2$ and both $K_1$ and $k_2$ indicating that although the $K_1$ and $k_2$ reductions are correlated $k_2$ is reduced more. Importantly, $k_2$ and $k_3$ are not strongly correlated, indicating that high $k_3$ is not being falsely attributed as low $k_2$ or *vice versa*. Although $k_3$ and $K_i$ are highly correlated ($r = 0.71$ to 0.85), increased $K_1/k_2$ could explain part of the increase in $K_i$ for the MCAo rat.

As the irreversible trapping rate can be related to tissue oxygen concentration (Casciari *et al*, 1995), $k_3$ is potentially a more specific measure of hypoxia than $K_i$. BAFPIC reduced the variability of $k_3$ to match that of $K_i$ in normoxic tissue, although it was still higher in hypoxic tissue. Further studies are warranted to determine which of $k_3$ and $K_i$ is the best *in vivo* measure of hypoxia, particularly for scenarios subject to changes in tissue influx/efflux which potentially compromise the ability of $K_i$ to quantify hypoxia. The stroke model used in this study is one example of this, others include tumour response to therapy studies. In addition to FMISO, mapping $k_3$ could be of interest for irreversible tracers such as the cellular proliferation marker [18F]fluorothymidine (de Langen *et al*, 2009), [11C]methionine used to image amino-acid metabolism (Buus *et al*, 2004), and FDG, although $K_i$ is usually the key parameter of interest for FDG because it can be converted to glucose metabolic rate. Parametric maps of $k_3$ produced by BAFPIC and/or the low variance $K_i$ maps produced by BAFPIC may be particularly useful if PET information is to be used in radiotherapy treatment planning (Alber *et al*, 2003; Rajendran *et al*, 2006).

In conclusion, simulations and real data have shown that in a rat model of cortical ischaemia, a basis function approach (BAFPIC) for kinetic modelling with an irreversible two-tissue compartment model provides superior FMISO parametric maps than NLLS solution for $K_1$, $k_2$, $k_3$, $V_b$, and both NLLS solution and PGA for $K_i$. BAFPIC is easy to implement, computationally efficient, and could be applied to other tracers in which an irreversible two-tissue compartment model is applicable, particularly those in which $k_3$ is a parameter of interest as well as $K_i$. Although the emphasis of this study has been on voxelwise modelling, BAFPIC will also be an attractive option for kinetic parameter estimation at the regional level if the regional TAC is noisy.

## Acknowledgements

We thank Drs M Takasawa, K Igase, and JL Hughes for their contribution to the experiments.

## Disclosure/conflict of interest

The authors declare no conflict of interest.

## References

Alber M, Paulsen F, Eschmann SM, Machulla HJ (2003) On biologically conformal boost dose optimization. *Phys Med Biol* 48:N31–5

Barrett HH, Wilson DW, Tsui BMW (1994) Noise properties of the EM algorithm: I. Theory. *Phys Med Biol* 39:833–46

Blomqvist G (1984) On the construction of functional maps in positron emission tomography. *J Cereb Blood Flow Metab* 4:629–32

Boellaard R, Knaapen P, Rijbroek A, Luurtsema GJJ, Lammertsma AA (2005) Evaluation of basis function and linear least squares methods for generating parametric blood flow images using $^{15}$O-water and positron emission tomography. *Mol Imaging Biol* 7:273–85

Bruehlmeier M, Roelcke U, Schubiger PA, Ametamey SM (2004) Assessment of hypoxia and perfusion in human brain tumours using PET with $^{18}$F-Fluoromisonidazole and $^{15}O$-$H_2O$. *J Nucl Med* 45:1851–9

Buus S, Grau C, Munk OL, Bender D, Jensen K, Keiding S (2004) $^{11}$C-methionine PET, a novel method for measuring regional salivary gland function after radiotherapy of head and neck cancer. *Radiother Oncol* 73:289–96

Casciari JJ, Graham MM, Rasey JS (1995) A modeling approach for quantifying tumor hypoxia with [18F]fluoromisonidazole PET time-activity data. *Med Phys* 22:1127–39

Chapman JD, Lee J, Meeker BE (1989) Keynote address: cellular reduction of nitromidazole drugs: potential for selective chemotherapy and diagnosis of hypoxic cells. *Int J Radiat Oncol Biol Phys* 16:911–7

de Langen AJ, Klabbers B, Lubberink M, Boellaard R, Spreeuwenberg MD, Slotman BJ, de Bree R, Smit EF, Hoekstra OS, Lammertsma AA (2009) Reproducibility of quantitative $^{18}$F-3′-deoxy-3′-fluorothymidine measurements using positron emission tomography. *Eur J Nucl Med Mol Imaging* 36:389–95

Eschmann SM, Paulsen F, Bedeshem C, Machulla HJ, Hehr T, Bamberg M, Bares R (2007) Hypoxia-imaging with $^{18}$F-misonidazole and PET: changes of kinetics during radiotherapy of head-and-neck cancer. *Radiother Oncol* 83:406–10

Feng D, Ho D, Chen K, Wu LC, Wang JK, Liu RS, Yeh SH (1995) An evaluation of the algorithms for determining local cerebral metabolic rates of glucose using positron emission tomography dynamic data. *IEEE Trans Med Imag* 14:697–710

Gjedde A (1982) Calculation of cerebral glucose phosphorylation from brain uptake of glucose analogs *in vivo*: a re-examination. *Brain Res Rev* 4:237–74

Gunn RN, Lammertsma AA, Hume SP, Cunningham VJ (1997) Parametric imaging of ligand-receptor binding in PET using a simplified reference region model. *NeuroImage* 6:279–87

Hong YT, Fryer TD (2010) Kinetic modelling using basis functions derived from two-tissue compartmental models with a plasma input function: general principle and application to [18F]fluorodeoxyglucose positron emission tomography. *NeuroImage* 51:164–72

Householder AS (1970) *The Numerical Treatment of a Single Non-Linear Equation*. New York, NY: McGraw-Hill

Huang X, Zhou Y, Bao S, Huang S-C (2007) Clustering-based linear least square fitting method for generation of parametric images in dynamic FDG PET studies. *Int J Biomed Imag* doi: 10.1155/2007/65641

Kelly CJ, Brady M (2006) A model to simulate tumour oxygenation and dynamic [18F]-FMISO PET data. *Phys Med Biol* 51:5859–73

Kimura Y, Senda M, Alpert NM (2002) Fast formation of statistically reliable FDG parametric images based on clustering and principal components. *Phys Med Biol* 47:455–68

Kinahan PE, Rogers JG (1989) Analytic 3D image reconstruction using all detected events. *IEEE Trans Nucl Sci* 36:964–8

Koeppe RA, Holden JE, Ip WR (1985) Performance comparison of parameter estimation techniques for the quantitation of local cerebral blood flow by dynamic positron computed tomography. *J Cereb Blood Flow Metab* 5:224–34

Koh W-J, Rasey JS, Evans ML, Grierson JR, Lewellen TK, Graham MM, Krohn KA, Griffin TW (1992) Imaging of hypoxia in human tumors with [F-18]fluoromisonidazole. *Int J Radiat Oncol Biol Phys* 22:199–212

Lodge MA, Carson RE, Carrasquillo JA, Whatley M, Libutti SK, Bacharach SL (2000) Parametric images of blood flow in oncology PET studies using [15O]water. *J Nucl Med* 41:1784–92

Logan J, Fowler JS, Volkow ND, Wolf AP, Dewey SL, Schlyer DJ, MacGregor RR, Hitzemann R, Bendriem B, Gatley SJ, Christman DR (1990) Graphical analysis of reversible radioligand binding from time-activity measurements applied to [*N*-11C-methyl]-(-)-cocaine PET studies in human subjects. *J Cereb Blood Flow Metab* 10:740–7

Markus R, Reutens DC, Kazui S, Read S, Wright P, Pearce DC, Tochon-Danguy HJ, Sachinidis JI, Donnan GA (2004) Hypoxic tissue in ischaemic stroke: persistence and clinical consequences of spontaneous survival. *Brain* 127:1427–36

Marquardt D (1963) An algorithm for least-squares estimation of non-linear parameters. *SIAM J Appl Math* 11:431–41

Martin GV, Caldwell JH, Graham MM, Grierson JR, Kroll K, Cowan MJ, Lewellen TK, Rasey JS, Casciari JJ, Krohn KA (1992) Noninvasive detection of hypoxic myocardium using fluorine-18-fluoromisonidazole and positron emission tomography. *J Nucl Med* 33:2202–8

Patlak CS, Blasberg RG, Fenstermacher JD (1983) Graphical evaluation of blood-to-brain transfer constants from multiple-time uptake data. *J Cereb Blood Flow Metab* 3:1–7

Rajendran JG, Hendrickson KRG, Spence AM, Muzi M, Krohn KA, Mankoff DA (2006) Hypoxia imaging-directed radiation treatment planning. *Eur J Nucl Med Mol Imaging* 33:S44–53

Rasey JS, Koh WJ, Evans ML, Peterson LM, Lewellen TK, Graham MM, Krohn KA (1996) Quantifying regional hypoxia in human tumors with positron emission tomography of [18F]fluoromisonidazole: a pre-therapy study of 37 patients. *Int J Radiat Oncol Biol Phys* 36:417–28

Spratt NJ, Donnan GA, Howells DW (2009) Characterisation of the timing of binding of the hypoxia tracer FMISO after stroke. *Brain Res* 1288:135–42

Tai YC, Chatziioannou A, Siegel S, Young J, Newport D, Goble RN, Nutt RE, Cherry SR (2001) Performance evaluation of the microPET P4: a PET system dedicated to animal imaging. *Phys Med Biol* 46:1845–62

Takasawa M, Beech JS, Fryer TD, Hong YT, Hughes JL, Igase K, Jones PS, Smith R, Aigbirhio FI, Menon DK, Clark JC, Baron JC (2007) Imaging of brain hypoxia in permanent and temporary middle cerebral artery occlusion in the rat using 18F-fluoromisonidazole and positron emission tomography: a pilot study. *J Cereb Blood Flow Metab* 27:679–89

Takasawa M, Moustafa RR, Baron JC (2008) Applications of nitromidazole *in vivo* hypoxia imaging in ischaemic stroke. *Stroke* 39:1629–37

Thorwarth D, Eschmann SM, Paulsen F, Alber M (2005) A kinetic model for dynamic [18F]-FMISO PET data to analyse tumour hypoxia. *Phys Med Biol* 50:2209–24

Thorwarth D, Eschmann SM, Holzner F, Paulsen F, Alber M (2006) Combined uptake of [18F]FDG and [18F]FMISO correlates with radiation therapy outcome in head-and-neck cancer patients. *Radiother Oncol* 80:151–6

Wang W, Georgi JC, Nehmeh SA, Narayanan M, Paulus T, Bal M, O'Donoghue J, Zanzonico PB, Schmidtlein CR, Lee NY, Humm JL (2009) Evaluation of a compartmental model for estimating tumor hypoxia via 18F-FMISO dynamic PET imaging. *Phys Med Biol* 54:3083–99

Wang W, Lee NY, Georgi J-C, Narayanan M, Guillem J, Schöder H, Humm JL (2010) Pharmacokinetic analysis of hypoxia 18F-fluoromisonidazole dynamic PET in head and neck cancer. *J Nucl Med* 51:37–45

Watabe H, Jino H, Kawachi N (2005) Parametric imaging of myocardial blood flow with 15O-water and PET using the basis function method. *J Nucl Med* 46:1219–24

Wu Y, Carson RE (2002) Noise reduction in the simplified reference tissue model for neuroreceptor functional imaging. *J Cereb Blood Flow Metab* 22:1440–52

Zhou Y, Huang S-C, Bergsneider M, Wong DF (2002) Improved parametric image generation using spatial-temporal analysis of dynamic PET studies. *NeuroImage* 15:697–707

Supplementary Information accompanies the paper on the Journal of Cerebral Blood Flow & Metabolism website (http://www.nature.com/jcbfm)